

ARTICLE OPEN



Scale-invariant machine-learning model accelerates the discovery of quaternary chalcogenides with ultralow lattice thermal conductivity

Koushik Pal^{1,2}, Cheol Woo Park^{1,2}, Yi Xia¹, Jiahong Shen¹ and Chris Wolverton¹

We design an advanced machine-learning (ML) model based on crystal graph convolutional neural network that is insensitive to volumes (i.e., scale) of the input crystal structures to discover novel quaternary chalcogenides, $AMM'Q_3$ ($A/M/M' =$ alkali, alkaline earth, post-transition metals, lanthanides, and $Q =$ chalcogens). These compounds are shown to possess ultralow lattice thermal conductivity (κ_l), a desired requirement for thermal-barrier coatings and thermoelectrics. Upon screening the thermodynamic stability of ~ 1 million compounds using the ML model iteratively and performing density-functional theory (DFT) calculations for a small fraction of compounds, we discover 99 compounds that are validated to be stable in DFT. Taking several DFT-stable compounds, we calculate their κ_l using Peierls–Boltzmann transport equation, which reveals ultralow κ_l ($< 2 \text{ W m}^{-1} \text{ K}^{-1}$ at room temperature) due to their soft elasticity and strong phonon anharmonicity. Our work demonstrates the high efficiency of scale-invariant ML model in predicting novel compounds and presents experimental-research opportunities with these new compounds.

npj Computational Materials (2022)8:48; <https://doi.org/10.1038/s41524-022-00732-8>

INTRODUCTION

The study of heat-transport phenomena in materials is imperative to find and deploy suitable materials in various thermal-energy management platforms such as thermal barrier coatings¹, waste-heat-recovery devices², and modern high-performance computing architectures that require rapid heat dissipation³. A sustained research effort in this direction has focused on finding materials with extreme thermal-transport properties^{3–8}. Among them, semiconducting materials with very low lattice thermal conductivity (κ_l) are particularly interesting as they find applications in thermoelectrics (TEs), which can convert heat into electrical energy^{9–11}. The TE conversion efficiency of materials, quantified by the figure of merit, $ZT = \frac{S^2 \sigma}{\kappa_l + \kappa_e} T$, can be enhanced by reducing their κ_l . In the preceding equation S , σ , and κ_e are the Seebeck coefficient, electrical conductivity, and electronic contribution to the total thermal conductivity ($\kappa = \kappa_l + \kappa_e$), respectively. Hence, novel compounds with intrinsically low κ_l are highly sought after for fundamental research that would help in the design and discovery of efficient materials suitable for device applications.

The discovery of novel compounds is an important yet challenging task in materials science. Traditionally, trial-and-error methods have been employed in the laboratory to synthesize new compounds. However, accurate quantum-mechanical methods such as density-functional theory (DFT) have proven to be extremely beneficial in the discovery of new materials and estimation of their properties, by reducing the target-composition space considered for exploratory synthesis in the laboratory. In the last few years, modern computational approaches such as high-throughput (HT) DFT calculations based on prototype decoration have accelerated the discovery of new compounds^{12–16}. These approaches take advantage of the computed energetics of a large number of materials available in diverse materials databases, such as the Open Quantum Materials Database (OQMD)^{14,17}, Materials Project¹⁵, and Aflowlib¹⁶, which

enable us to perform a highly accurate phase-stability analysis of a novel compound taking into account all of its competing phases.

In the HT-DFT method, the initial crystal structures are generated by decorating prototype crystal structures with elements from the periodic table. To keep the number of calculations of generated compounds computationally tractable, we often use certain rules during prototype decoration, which are typically derived from examining the already-known compounds in that family. For example, (a) chemically similar elements are substituted at each crystallographically inequivalent site in the prototype structures and (b) only those compositions that balance the valence charges of the elements are generated. While these considerations often lead to a high success rate in predicting stable compounds, it leaves out a large number of other “unsuspected” compounds that would be generated if we substitute all elements from the periodic table in any sites of the prototype structures in all possible combinations. Therefore, we suffer the risk of missing out perhaps many hitherto unknown stable compounds that could exhibit exciting physical and chemical properties.

Machine learning (ML) offers a computationally feasible solution to this problem. Using ML methods, the entire phase space of multinary compositions can be quickly screened for possible stable and metastable compounds even before doing any expensive DFT calculations. In recent years, ML methods have proven to be an invaluable tool in discovering novel compounds in multicomponent composition spaces^{18–27}. In one successful example, Ren et al.²⁸ predicted new stable bulk metallic glasses using an ML model and were able to experimentally synthesize them. Another interesting example of ML-guided materials discovery is demonstrated in the work by Kim et al.²⁹ where they predicted several new stable quaternary Heuslers (QH). In their work, Kim et al. generated nearly 3.3 million quaternary compositions in the Heusler structure by substituting 73 metallic

¹Department of Materials Science and Engineering, Northwestern University, Evanston, IL 60208, USA. ²These authors contributed equally: Koushik Pal, Cheol Woo Park. ✉email: koushik.pal.physics@gmail.com; cheolpark2016@u.northwestern.edu; c-wolverton@northwestern.edu

elements from the periodic table at the three inequivalent crystallographic sites in every possible way. An ML model was constructed, which was trained on the computed energetics of compounds available in the OQMD to assess the phase stability of those 3.3 million compositions. The ML-predicted stable compounds were then validated by performing DFT calculations, which gave rise to 55 new DFT-stable compounds that were missing from the earlier HT-DFT^{30,31} and ML²⁵ works in the same Heusler family, as those previous works only explored a smaller set of compositions restricted by the electron-counting and charge-neutrality conditions.

In this work, we use an ML method to explore the vast phase space spanned by a family of experimentally known quaternary chalcogenides (AMM'Q₃)^{32–39} that possess diverse structure types and chemistry. Some of these compounds are shown to exhibit very low lattice thermal conductivity^{40,41}, promising thermoelectric performance^{42,43}, and high photovoltaic efficiency⁴⁴. In our previous HT search⁴⁵ for new materials in this crystal family, we discovered a large number (628) of stable compounds. However, our previous search⁴⁵ explored only a small set of possible compositions since we generated the initial crystal structures of the compounds following a set of rules that were derived by examining all experimentally known AMM'Q₃ compounds. They are: (a) All elements in the AMM'Q₃ compounds are in their most common oxidation states that satisfy the valence–charge-neutrality condition, (b) the A-site is occupied by alkali, alkaline-earth, or post-transition metals with the only exception of Eu that is a lanthanide, (c) the M-site is occupied by transition metals, (d) the M' site is occupied by transition metals or lanthanides, (e) Q-site is always occupied by S, Se, or Te, and (f) no compounds contain more than one alkali and alkaline-earth metals or a combination of them. Adhering to these criteria, we generated 4659 unique charge-balanced compositions and performed HT-DFT calculations considering all structural prototypes that are known in this family of compounds, leading to the discovery of 628 stable and 852 low-energy metastable compounds in our previous work⁴⁵.

Thus, the chemical trends that can be observed from the experimentally known AMM'Q₃ compounds served as a useful guide to discover previously unknown stable compounds in this family of materials. However, in this study, we are interested in identifying new stable compositions in the AMM'Q₃ prototypes that do not necessarily follow those chemical criteria and therefore, were overlooked in the previous HT-DFT search⁴⁵. For an exhaustive search of the phase space, in this work, we generate the initial quaternary compositions that do not necessarily follow the previous rules. Here, 66 metallic elements are considered for substitutions at the A, M, and M' cation sites in every possible way while generating the initial structures. Keeping the Q atoms fixed to three chalcogens (S, Se, and Te), we generate a total number of 823,680 (=3 × 66P₃) initial compositions of these quaternary chalcogenides, which is the target search space in this work.

To this end, we develop an advanced ML framework based on the recently proposed iCGCNN framework⁴⁶, a variant model of the crystal-graph convolutional neural network (CGCNN)⁴⁷. Conventionally, machine-learning (ML) models were constructed based on compositional features of the compounds that have limited predictive ability⁴⁸. Recent developments showed that structure-based ML model such as the CGCNN⁴⁷ provides a significant improvement in the prediction of properties of compounds based on their crystal geometries. In the iCGCNN framework, crystal structures are represented as crystal graphs that are then used as input for graph neural networks to predict material properties of interest. Although iCGCNN has been shown to exhibit high accuracy in predicting the formation energy, a property directly relevant to the thermodynamic stability of a material, here, we show that iCGCNN exhibits peak performance when the input crystal structures are fully relaxed in terms of

volume, stress, and ionic positions. This dependency can limit the effectiveness of the ML models in situations where the relaxed crystal structures are unavailable. This situation can arise when prior HT-DFT data for a class of materials do not exist. For our ML model used in this study, we designed it, such that the formation energy predictions are invariant to the volumes (i.e., scale) of the input crystal structures to account for the fact that unrelaxed crystal structures can have arbitrary volumes. We show that our ML model outperforms the iCGCNN model by 25% in predicting the formation energies of materials when provided with the unrelaxed crystal structures as input.

With the iterative use of the ML model on the 823,680 newly generated compounds combined with successive filtering and DFT calculations, we discover hitherto unknown 99 DFT-stable and 362 low-energy DFT-metastable compounds that are potentially synthesizable in the laboratory. Of the newly discovered 99 stable compounds, we randomly chose 14 compounds that are semiconducting and nonmagnetic to examine their thermal-transport properties by solving the Peierls-Boltzmann transport equation (PBTE) in a first-principles framework. The newly discovered compounds in this work are validated by DFT, that possess ultralow κ_l , and have “unsuspected” combination of elements, and hence are different from those predicted in a previous HT-DFT work⁴⁵.

RESULTS

Scale-invariant machine-learning model

We design our ML model based on iCGCNN, a variant model of the CGCNN^{46,47}. In iCGCNN, the unit cell of a compound is represented as a crystal graph $\mathcal{G} = (\mathcal{N}, \mathcal{E})$, where node $n_i \in \mathcal{N}$ represents constituent atom i and edge $e_{(ij)_k} \in \mathcal{E}$ represents the bond between atom i and neighboring atom j . Atoms are considered neighbors if they share a face in the Voronoi tessellated crystal structure. To account for the periodicity of the crystal, multiple edges can exist between neighboring nodes as indexed by k . Node n_i is then embedded with vector \mathbf{v}_i that encodes the elemental properties of atom i , where embedding is defined as the mapping of a discrete object to a vector of real numbers. Edge $e_{(ij)_k} \in \mathcal{E}$ is also embedded with vector $\mathbf{u}_{(ij)_k} \in \mathcal{E}$ that encodes the structural information of the polyhedra formed by neighboring atoms i and j , and their shared Voronoi face. Structural information encoded in $\mathbf{u}_{(ij)_k} \in \mathcal{E}$ includes the interatomic distance between atoms i and j , solid angle of atom i with respect to the shared Voronoi face, area of the shared Voronoi face, and volume of the polyhedra. This crystal graph is then used as direct input to a graph neural network where the node and edge embeddings are iteratively updated according to predefined convolution functions. The convolution functions for the node (f_v^t) and edge (f_u^t) embeddings at the t th iteration are given by

$$f_v^t : \mathbf{v}_i^{(t+1)} = \mathbf{v}_i^{(t)} + \sum_{(j,k)} \sigma(\mathbf{z}_{(ij)_k}^{(t)} \mathbf{W}_1^{(t)} + \mathbf{b}_1^{(t)}) \odot g(\mathbf{z}_{(ij)_k}^{(t)} \mathbf{W}_2^{(t)} + \mathbf{b}_2^{(t)}) + \sum_{(j,l,k,k')} \sigma(\mathbf{z}_{(ij,l)(k,k')}^{(t)} \mathbf{W}_1'^{(t)} + \mathbf{b}_1'^{(t)}) \odot g(\mathbf{z}_{(ij,l)(k,k')}^{(t)} \mathbf{W}_2'^{(t)} + \mathbf{b}_2'^{(t)}) \quad (1)$$

$$f_u^t : \mathbf{u}_{(ij)_k}^{(t+1)} = \mathbf{u}_{(ij)_k}^{(t)} + \sum_{(j,k)} \sigma(\mathbf{z}_{(ij)_k}^{(t)} \mathbf{W}_1^{(t)} + \mathbf{b}_1^{(t)}) \odot g(\mathbf{z}_{(ij)_k}^{(t)} \mathbf{W}_2^{(t)} + \mathbf{b}_2^{(t)}) + \sum_{(j,l,k,k')} \sigma(\mathbf{z}_{(ij,l)(k,k')}^{(t)} \mathbf{W}_1'^{(t)} + \mathbf{b}_1'^{(t)}) \odot g(\mathbf{z}_{(ij,l)(k,k')}^{(t)} \mathbf{W}_2'^{(t)} + \mathbf{b}_2'^{(t)}) \quad (2)$$

In the above equations, \odot represents an element-wise matrix multiplication, while σ and g represent a sigmoid function and a nonlinear activation function, respectively. $\mathbf{W}^{(t)}$ ($\mathbf{W}'^{(t)}$) and $\mathbf{b}^{(t)}$ ($\mathbf{b}'^{(t)}$) represent the weight and bias matrices, respectively, for the t th convolution step. $\mathbf{z}_{(ij)_k}^{(t)} = \mathbf{v}_i^{(t)} \oplus \mathbf{v}_j^{(t)} \oplus \mathbf{u}_{(ij)_k}^{(t)}$ is the concatenation

Table 1. Performance test of the machine-learning models under four different conditions. The performances of CGCNN, iCGCNN, and the newly implemented ML model in predicting the formation energy of 230,000 materials in the test set are shown with respect to how relaxed the input crystal structures are prior to constructing the crystal graphs.

ML-models	Condition #1: fully relaxed (meV/atom)	Condition #2: unrelaxed (meV/atom)	Condition #3: unrelaxed, but rescaled to have relaxed volume (meV/atom)	Condition #4: unrelaxed, but rescaled to have volume predicted by Magpie [49] (meV/atom)
CGCNN [47]	41.3	72.2	48.8	59.6
iCGCNN [46]	30.1	62.3	40.2	49.2
This work	42.7	46.5	46.5	46.5

of the node and edge vectors and captures the two-body correlation of atoms i and j . Likewise, the node vectors and edge vectors that connect atoms i , j , and l are concatenated to form $\mathbf{z}_{(i,j,l)(k,k')}^{(t)} = \mathbf{v}_i^{(t)} \oplus \mathbf{v}_j^{(t)} \oplus \mathbf{v}_l^{(t)} \oplus \mathbf{u}_{(ij)_k}^{(t)} \oplus \mathbf{u}_{(ij)_k'}^{(t)}$ to capture the three-body correlations of the atoms. After each iteration of convolution, the node and edge embeddings are updated to better represent the local chemical environments of the atoms and bonds. At the end of the convolution steps, a pooling layer is used to generate an overall feature vector \mathbf{v}_c for the crystal structure by taking the normalized sum of the final node embeddings \mathbf{v}_i^f . Mathematically, \mathbf{v}_c can be written as

$$\mathbf{v}_c = \frac{1}{N} \sum_i \mathbf{v}_i^f, \quad (3)$$

where N represents the number of atoms in the unit cell of the crystal structure. This feature vector is then used as a direct input for a neural network hidden layer to predict the material property of interest which, in our study, is the formation energy.

Although iCGCNN has been shown to achieve state-of-the-art accuracy in predicting the formation energies of inorganic materials⁴⁶, such performance requires the crystal structures to be fully relaxed in terms of volume, stress, and ionic positions prior to constructing the crystal graphs. When the relaxed crystal structures are unavailable, the model performance can vary, depending on how closely the unrelaxed structures resemble their respective relaxed states. To illustrate, we measured the performance of iCGCNN under four different conditions. In all conditions, the ML model was trained on 200,000 formation-energy entries randomly chosen from the OQMD, where the training crystal graphs were generated based on the DFT-relaxed crystal structures. However, when testing the model on another 230,000 entries, the crystal structures that were used to construct the testing crystal graphs in each condition differed in terms of their state of relaxation. In Condition #1, fully relaxed crystal structures were used to construct the crystal graphs of the test set, while in Condition #2, the unrelaxed crystal structures that serve as input for the DFT calculations were used. For Condition #3, we used the crystal structures that have been relaxed in terms of volume, but not in terms of stress or ionic positions. These structures were obtained by rescaling the unrelaxed crystal structures from Condition #2 such that their volume is equivalent to that of the fully relaxed crystal structures from Condition #1. For an additional benchmark, we trained a Magpie model¹⁹ that incorporates the Voronoi tessellation attributes⁴⁹ to predict the volume of the compounds in the test set. For training, the relaxed structures were used to generate the Voronoi tessellation attributes. Voronoi tessellation attributes of the unrelaxed crystal structures were used for the volume prediction of the test data. The error of the Magpie model in predicting the volume of the crystal structures in the test data was 0.527 Å³ per atom. In Condition #4, we rescaled the unrelaxed crystal structures from Condition #2 to the volume predicted by the Magpie model prior to constructing the crystal graphs.

The performance of iCGCNN under these testing conditions is summarized in Table 1, and the relevant figures are shown in Supplementary Fig. 1. Under Condition #2, the mean absolute error (MAE) was 62.3 meV/atom. This is still significantly lower than the DFT error for experimentally measured formation energies (~100 meV/atom)¹⁷ of inorganic compounds, showing that iCGCNN remains a reliable method to predict DFT-calculated formation energies even when provided with the unrelaxed crystal structures. However, compared with the MAE of 30.1 meV/atom, when the fully relaxed crystal structures were used, the error for Condition #2 increased more than twofold, indicating that the ML model is unable to perform at its peak capability when the relaxed structures are unavailable such as in a high-throughput DFT search for new materials. Under Conditions #3 and #4, the MAE's were respectively 40.2 and 49.0 meV/atom which are 35% and 21% lower than that of Condition #2. This shows that when provided with unrelaxed crystal structures as input, iCGCNN performs better the closer the volumes of the structures are to their relaxed values. This further implies that iCGCNN significantly depends on the crystal-volume information when predicting the formation energy of materials.

Here, we describe a variant iCGCNN model, illustrated in Fig. 1, that independently generates the relaxed crystal-volume information needed to more accurately predict the formation energy of materials when provided with the unrelaxed crystal structures as input. This is achieved through a multiobjective framework in which the ML model simultaneously predicts the relaxed volume and formation energies of the crystals. This enables the information that is used in predicting the relaxed volumes to also be utilized in predicting the formation energies and vice versa. In this improved ML framework, before constructing the crystal graph, we normalized the crystal structures that have been provided as input for the ML model to take into account the fact that an unrelaxed crystal structure can have an arbitrary volume. The normalization process involves dividing the lattice parameters a , b , and c of the unit cell by the minimum interatomic distance measured within the provided input crystal structure, such that the minimum interatomic distance measured within the resulting normalized structure becomes 1. Note that during the normalization process, the fractional coordinates of the atoms with respect to the lattice vectors remain unchanged. As in iCGCNN, the normalized structure is then represented as a crystal graph where each node n_i is connected to the nodes that represent the Voronoi neighbors of atom i . Also, node n_i is embedded with vector \mathbf{v}_i to represent the atomic properties of atom i , and edge $\mathbf{e}_{(ij)_k}$ is embedded with vector $\mathbf{u}_{(ij)_k}$ to represent the structural properties of the normalized Voronoi polyhedral formed by atoms i and j .

Associated to the nodes and edges, each crystal graph is associated with a scale factor s , a scalar quantity that represents the minimum interatomic distance of the crystal structure. Since the structures are normalized to have a minimum interatomic distance of 1 prior to constructing the crystal graphs, the initial value of the scale factor, s^0 , is 1 for all crystal graphs. During the convolution steps, s is iteratively updated as a function of the

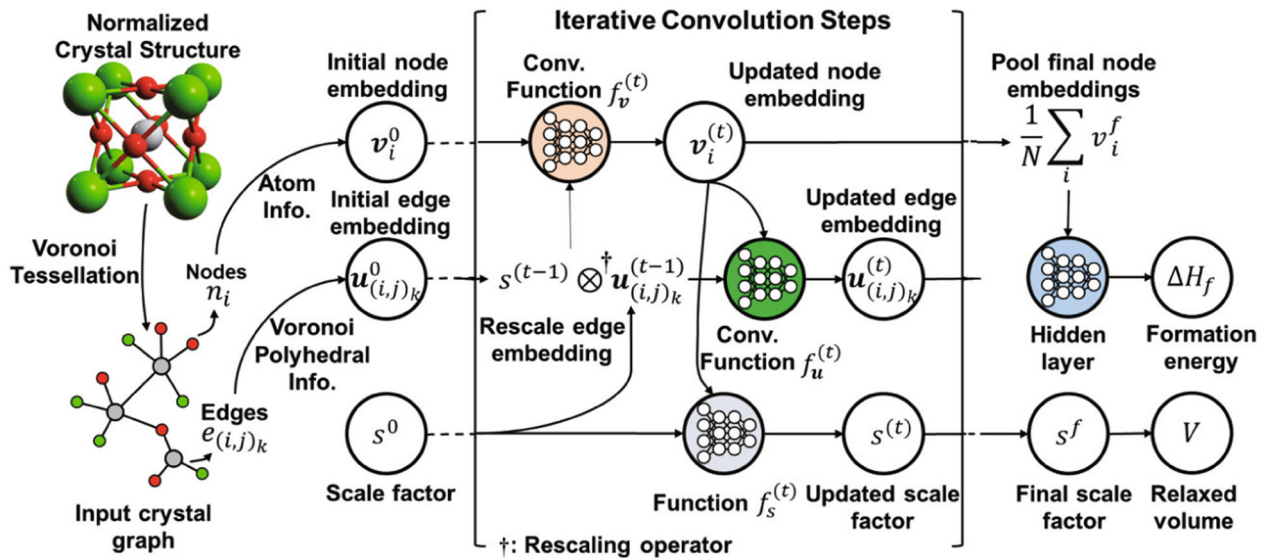


Fig. 1 Schematic design of the machine-learning model. Illustration of the iCGCNN-based multiobjective ML framework that predicts both formation energy and relaxed volume of a crystal. The crystal graph is constructed from the Voronoi tessellated crystal structure that has been normalized to have a minimum interatomic distance of 1. Additional to the node and edge embeddings, \mathbf{v}_i and $\mathbf{u}_{(i,j)_k}$, that encode the atom and bond information, the crystal graph is associated with scale factor s that represents the minimum interatomic distance of the crystal. In each iterative convolution step, s is updated as a function of \mathbf{v}_i such that, at the end of all iterations, the final value s^f matches the minimum interatomic distance that would be measured in the crystal structure that has been relaxed with respect to volume. \mathbf{v}_i and $\mathbf{u}_{(i,j)_k}$ are also iteratively updated to better represent the local chemical environment of the crystal. Formation energy is predicted from the final node embedding \mathbf{v}_i^f and relaxed volume of the crystal is calculated by multiplying the cube of s^f with the volume of the normalized crystal structure.

node embeddings. At the t th convolution step, the update function for s can mathematically be written out as

$$f_s^t : s_i^{(t+1)} = \frac{1}{N} \sum_i (\mathbf{v}_i^{(t)} \mathbf{W}_3^{(t)} + \mathbf{b}_3^{(t)}) \quad (4)$$

where $\mathbf{W}_3^{(t)}$ and $\mathbf{b}_3^{(t)}$ represent the weight and bias of a neural network hidden layer that has a scalar output. s is updated, such that at the end of the convolution steps, the final value s^f matches the minimum interatomic distance that would be measured in the crystal structure that has been relaxed in terms of its volume. The relaxed volume of the compound can then be predicted by simply multiplying the cube of s^f to the volume of the normalized crystal structure.

The convolution functions for updating the node and edge embeddings, \mathbf{v}_i and $\mathbf{u}_{(i,j)_k}$ remain the same as in iCGCNN with the exception of the many-body correlation terms, $\mathbf{z}_{(i,j)_k}^{(t)}$ and $\mathbf{z}_{(i,j,l)(k,k')}^{(t)}$. For our framework, these terms are defined as $\mathbf{z}_{(i,j)_k}^{(t)} = \mathbf{v}_i^{(t)} \oplus \mathbf{v}_j^{(t)} \oplus (s^{(t)} \otimes \mathbf{u}_{(i,j)_k}^{(t)})$ and $\mathbf{z}_{(i,j,l)(k,k')}^{(t)} = \mathbf{v}_i^{(t)} \oplus \mathbf{v}_j^{(t)} \oplus \mathbf{v}_l^{(t)} \oplus (s^{(t)} \otimes \mathbf{u}_{(i,j)_k}^{(t)}) \oplus (s^{(t)} \otimes \mathbf{u}_{(i,l)_k'}^{(t)})$ where \otimes represents a rescaling operation. In the rescaling operation, each vector element of $\mathbf{u}_{(i,j)_k}^{(t)}$ is multiplied by $s^{(t)d}$, where the exponent d represents the dimension of structural feature that is encoded in the vector element. For example, if a vector element encodes information of the area of the Voronoi surface shared by two neighboring atoms, we multiply it by $s^{(t)2}$. However, vector elements that encode the solid-angle information remain unchanged during this operation. Such rescaling operation enables information used in predicting the relaxed volumes, specifically $s^{(t)}$, to be utilized by the node and edge embeddings in predicting the relaxed formation energies of materials. We note that while the model has been designed to predict the relaxed formation energies of materials based on their unrelaxed crystal structures, the model is trained explicitly on the relaxed crystal

structures and relaxed formation energies of compounds in the training data.

Using the previous illustration, we characterize and compare the performance of our ML model with respect to iCGCNN. As shown in Table 1, the MAE of our model under Condition #1 was 42.7 meV/atom, indicating that when the relaxed crystal structures are provided as input, iCGCNN outperforms the newly implemented model by 30%. This is because our model, unlike iCGCNN, is insensitive to the volume of the input crystal structure and thus, when provided with the relaxed volume information, is unable to take advantage of it as much as iCGCNN. The same reasoning can be used to explain why iCGCNN outperforms our model by 14% under Condition #3. However, under Condition #2, our model achieved an MAE of 46.5 meV/atom, which is 25% lower than iCGCNN. This shows that the new model performs significantly better than iCGCNN when the unrelaxed crystal structures are provided as input, suggesting that our model can more effectively assist in a high-throughput search for new materials even when there are fewer DFT-optimized crystal structures available for training the model. The error of our model is also lower than that of the iCGCNN model in Condition #4, indicating that our model improves upon existing ML methods in predicting the formation energy of materials. This improvement is most likely because the error of our model in predicting the volume of the crystal structures is 0.393 Å³ per atom, which is lower than the error of the Magpie model (0.527 Å³ per atom). The MAE of our model under Conditions #2, #3, and #4 is equal as expected since, by construction, the model predictions are invariant to the volume of the input crystal structures. While our model accounts for the volume differences between the relaxed and unrelaxed structures of crystal compounds, it does not account for the stress and ionic-position differences that occur during relaxation. Thus, the model is expected to perform less efficiently when there is a significant difference in the unit-cell shape or the ionic positions between the relaxed and unrelaxed crystal structures.

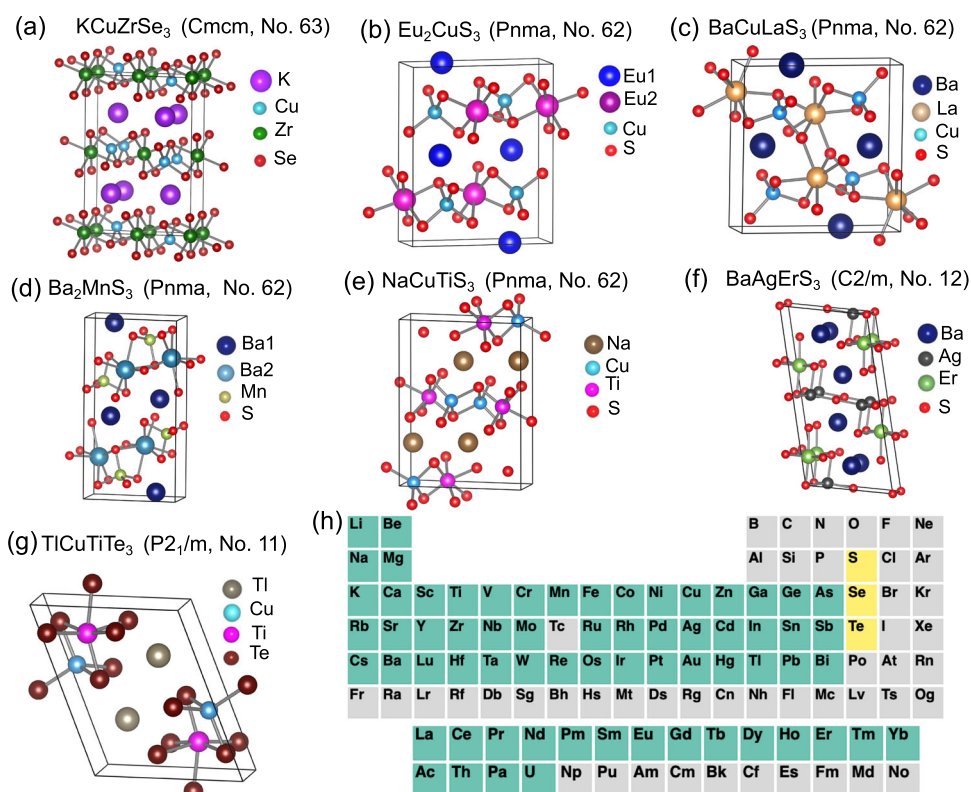


Fig. 2 Structural prototypes and elements used for novel material design. a–g Conventional unit cells of the seven crystallographic prototypes that are experimentally known in the family of $\text{AMM}'\text{Q}_3$ chalcogenides are shown. We have used these crystal structures for the design and discovery of new materials. h We have color-coded the 66 metallic elements (highlighted in green) in a periodic table that are substituted at the A, M-, and M'-cation sites in all possible combinations to generate the initial crystal structures of the new compounds. During prototype decoration, only three chalcogen atoms (highlighted in yellow) are substituted at the Q-sites.

While our model is heavily influenced by CGCNN, our model is different in that it not only incorporates the additional structural and many-body correlation information as implemented by iCGCNN, but it also normalizes the input crystal structures prior to constructing the crystal graphs, such that the ML predictions are independent of the volume of the input structures. To illustrate the improvements that result from these differences, we conducted the same tests under the four different conditions for the CGCNN model. As shown in Table 1, we find that our model outperforms the original CGCNN model⁴⁷ where the MAE of our model is lower by 55% when the input crystal structures are unrelaxed (Condition #2).

Design and discovery of new materials

The experimentally known $\text{AMM}'\text{Q}_3$ compounds^{32–39} crystallize in seven structural prototypes (Fig. 2) in four different space groups (SGs): KCuZrSe_3 (SG: Cmcm, No. 63), Eu_2CuS_3 (SG: Pnma, No. 62), BaCuLaS_3 (SG: Pnma, No. 62), Ba_2MnS_3 (SG: Pnma, No. 62), NaCuTiS_3 (SG: Pnma, No. 62), BaAgErS_3 (SG: C2/m, No. 12), and TiCuTiTe_3 (SG: $P2_1/m$, No. 11), most of which are layered and related to each other via structural distortions³². Among these, KCuZrSe_3 has the highest symmetry that constitutes 71% of the known $\text{AMM}'\text{Q}_3$ compounds⁴⁵. We note that while KCuZrSe_3 , BaAgErS_3 , and TiCuTiTe_3 have 12 atoms in their primitive unit cells, the rest of the structure types have 24 atoms. In Eu_2CuS_3 and Ba_2MnS_3 , Ba and Eu atoms occupy two distinct crystallographic sites in their crystal structures, respectively. It is worth mentioning that the three cations (A, M, and M') occupy different crystallographic sites in the crystal structures.

First, we generate the target search space of the initial quaternary compositions taking the KCuZrSe_3 structure type. We

chose this structure type as it is the most common in this family and all experimentally known $\text{AMM}'\text{Q}_3$ have low energies (within 50 meV/atom above the convex hull) in this prototype⁴⁵. We substitute 66 metallic elements (see Fig. 2h) available in the OQMD at the K-, Cu-, and Zr-sites in all possible combinations while keeping the Q-site fixed only to the chalcogens (S, Se, and Te). Thus, our search space contains a total number of ${}^{66}\text{P}_3 \times 3 = 823,680$ distinct compounds. Next, we use the newly designed ML model to predict 8370 stable quaternary chalcogenides with the ML-predicted hull distances (E_{hd}) being equal to zero. In the next step, we filter out compounds having radioactive elements and compounds that were already discovered before⁴⁵. Our final set contains 4199 unique compounds in the KCuZrSe_3 structure type for which we performed DFT calculations to validate the ML predictions. After performing $T = 0\text{K}$ thermodynamic phase-stability analysis on these compounds utilizing the data available in the OQMD, we retain ~1400 low-energy compounds whose E_{hd} lie within 50 meV/atom above the convex hull. It is worth noting the high success rate (33%) of our ML model compared with, e.g., the studies by (a) Kim et al.²⁹, where the authors validated 55 new quaternary Heusler compositions to be stable according to DFT calculations after predicting 303 stable compositions using their ML model, which translates to a success rate of 18% and (b) Faber et al.²⁰, where the authors predicted 2133 hypothetical elpasolite compounds to be stable through ML, out of which 128 of them turned out to be DFT-stable, which indicates a success rate of 6%.

In the next step, we take these 1400 compositions and generate their crystal structures in the other six structural prototypes known in the $\text{AMM}'\text{Q}_3$ family of compounds. We use the ML model again to predict stable compounds in these 1400 compositions among all structure types, which gave 800 ML-predicted stable quaternary compounds. We perform DFT calculations on these 800

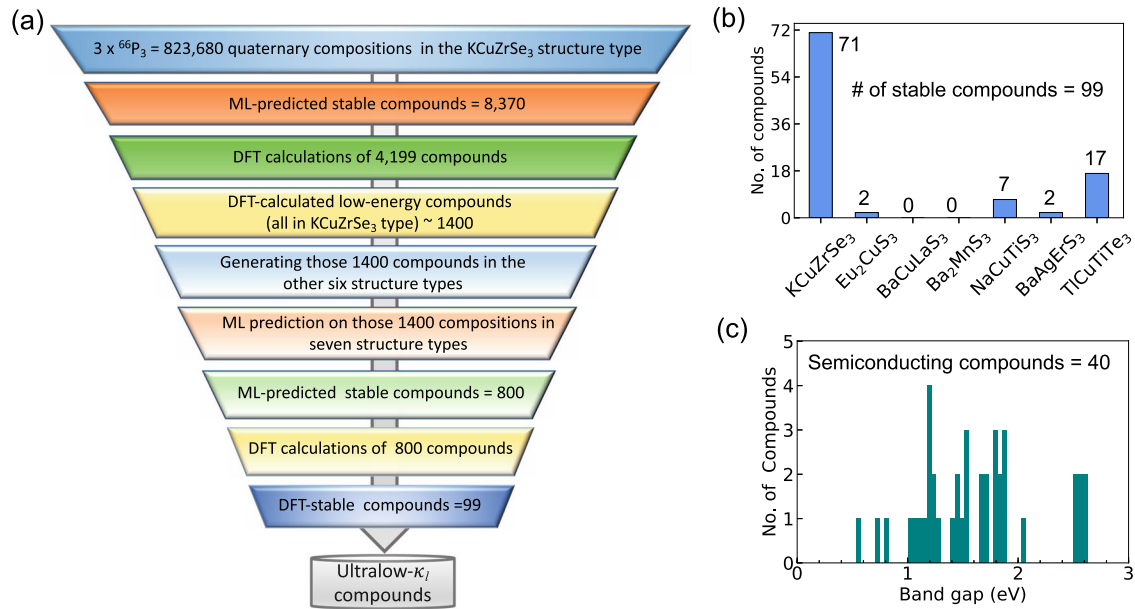


Fig. 3 Machine-learning assisted discovery of novel materials. **a** Schematic workflow of novel materials' discovery with iterative use of the machine-learning (ML) method and density-functional theory (DFT) calculations. The stable and metastable compounds are defined by their hull distance of ($E_{\text{hd}} = 0$ and $0 < E_{\text{hd}} \leq 50$ meV/atom, respectively). **b** The distribution of predicted stable compounds into seven structure types. **c** Histogram plot showing the distribution of the bandgaps of the predicted stable quaternary chalcogenides.

compounds and evaluate their $T = 0\text{K}$ thermodynamic phase stability in the OQMD. Finally, we discover 99 stable ($E_{\text{hd}} = 0$) and 362 low-energy metastable ($0 < E_{\text{hd}} \leq 50$ meV/atom) compounds having different structure types. A schematic funnel diagram of the material design and discovery is shown in Fig. 3a. We list these stable and metastable compounds with their energetic information in Supplementary Note 2. We also note that these compounds are distinct from the compounds that were predicted in the previous HT-DFT work⁴⁵. Our analysis reveals that among the 99 newly predicted stable compounds, 71 crystallize in the KCuZrSe₃ structure type followed by 17 compounds crystallizing in the TiCuTiTe₃ prototype (Fig. 3b). The other 11 compounds are found in Eu₂CuS₃ (2), NaCuTiS₃ (7), and BaAgErS₃ (2) structure types. We found no stable compounds in the BaCuLaS₃ and Ba₂MnS₃ prototypes. Analysis of the DFT-calculated band gap reveals that 40 of the 99 predicted stable compounds have finite bandgaps that vary between 0.53 eV and 2.63 eV, which is shown as a histogram plot in Fig. 3c.

We further analyze the newly predicted stable compounds in terms of the constituent elements (see bar charts in Fig. 4). The newly predicted 99 stable compounds consist of 23 sulfides, 40 selenides, and 36 tellurides. We note that the elements in all the predicted compounds are arranged to be in the A-M-M'-Q order as in the experimentally known AMM/Q₃ compounds to follow their site occupancy. This helps us identify which elements and chemical groups occupy the A, M, and M' sites. We notice that some of the predicted stable compounds do not appear to be charge-balanced, assuming the nominal oxidation states of the constituent elements, e.g., NaMnZrS₃, NaNiTiSe₃. We also see that the M-site in some of the sulfides and selenides is occupied by alkali metal (Li), e.g., in KLiZrS₃ and KLiZrSe₃. The M-site in some of the selenides is also occupied by alkaline-earth (e.g., CsMgYSe₃) or post-transition metals (e.g., CsSnYSe₃). Similarly, for tellurides, the M-site is sometimes occupied by an alkaline-earth metal, e.g., CsMgGdTe₃, or post-transition metal, e.g., KPbHoTe₃. The M'-site in some of the tellurides is occupied by post-transition metals, e.g., CsHgBiTe₃. It is also evident that some of the predicted stable compounds have a combination of alkali and alkaline-earth metals (e.g., KMgHoTe₃) and more than one alkali metal (e.g., KLiHfS₃).

These chemical trends are unique to these newly discovered compounds and are absent in the experimentally known^{32–39} and the previously⁴⁵ discovered AMM/Q₃ compounds.

Thermal-transport properties

We now investigate the thermal-transport properties of the newly discovered quaternary chalcogenides. To this end, we focus on the compounds that are nonmagnetic and semiconducting to unravel how the crystal structures influence their phonon dispersions and κ_l . We did not choose any magnetic as well as metallic compounds for this purpose as they can have significant magnonic and electronic contributions, respectively, to the total thermal conductivity (κ) as opposed to semiconductors where κ_l dominates κ . Further, we select only those compounds that have the KCuZrSe₃ structure type as it has the highest symmetry and the smallest unit cell among the seven structural prototypes known in this family of compounds. This choice makes the calculation of κ_l computationally less expensive compared with the other structure types. Since the calculation of κ_l within a first-principles framework is computationally very expensive, we randomly chose a set of 14 compounds from the list of predicted DFT-stable semiconducting chalcogenides and calculated their κ_l using PBTE as detailed in the “Methods” section. We calculate their electronic structures (see Supplementary Fig. 2), phonon dispersions (see Supplementary Fig. 3), and κ_l (Fig. 5). The DFT-calculated bandgaps (E_g) of these selected compounds vary from small (0.36 eV in CePdYSe₃) to large (2.43 eV in CsMgGdSe₃) values. From Fig. 5, it is seen that these compounds exhibit very low κ_l ($\kappa_l^{\perp} \leq 1.80$ Wm⁻¹K⁻¹ and $\kappa_l^{\parallel} \leq 0.50$ Wm⁻¹K⁻¹ at $T \geq 300$ K for any compounds), which is smaller than the values reported experimentally in single-crystalline SnSe ($\kappa_l^{\perp} \sim 1.90$ Wm⁻¹K⁻¹ and $\kappa_l^{\parallel} \sim 0.90$ Wm⁻¹K⁻¹ at $T = 300$ K)⁵⁰. Here, κ_l^{\perp} and κ_l^{\parallel} are the components that are perpendicular and parallel to the stacking direction in the crystal structure of the compounds, respectively. Due to the layered crystal structure, these two components of κ_l are strongly anisotropic with the κ_l^{\perp} being much larger than the κ_l^{\parallel} due to the stronger intralayer interactions. Among these 14 compounds, KLiHfS₃ has the highest (κ_l^{\perp} : 1.80 Wm⁻¹K⁻¹, κ_l^{\parallel} : 0.50 Wm⁻¹K⁻¹) and CsMgPrTe₃ has the lowest (κ_l^{\perp} : 0.67 Wm⁻¹K⁻¹, κ_l^{\parallel} :

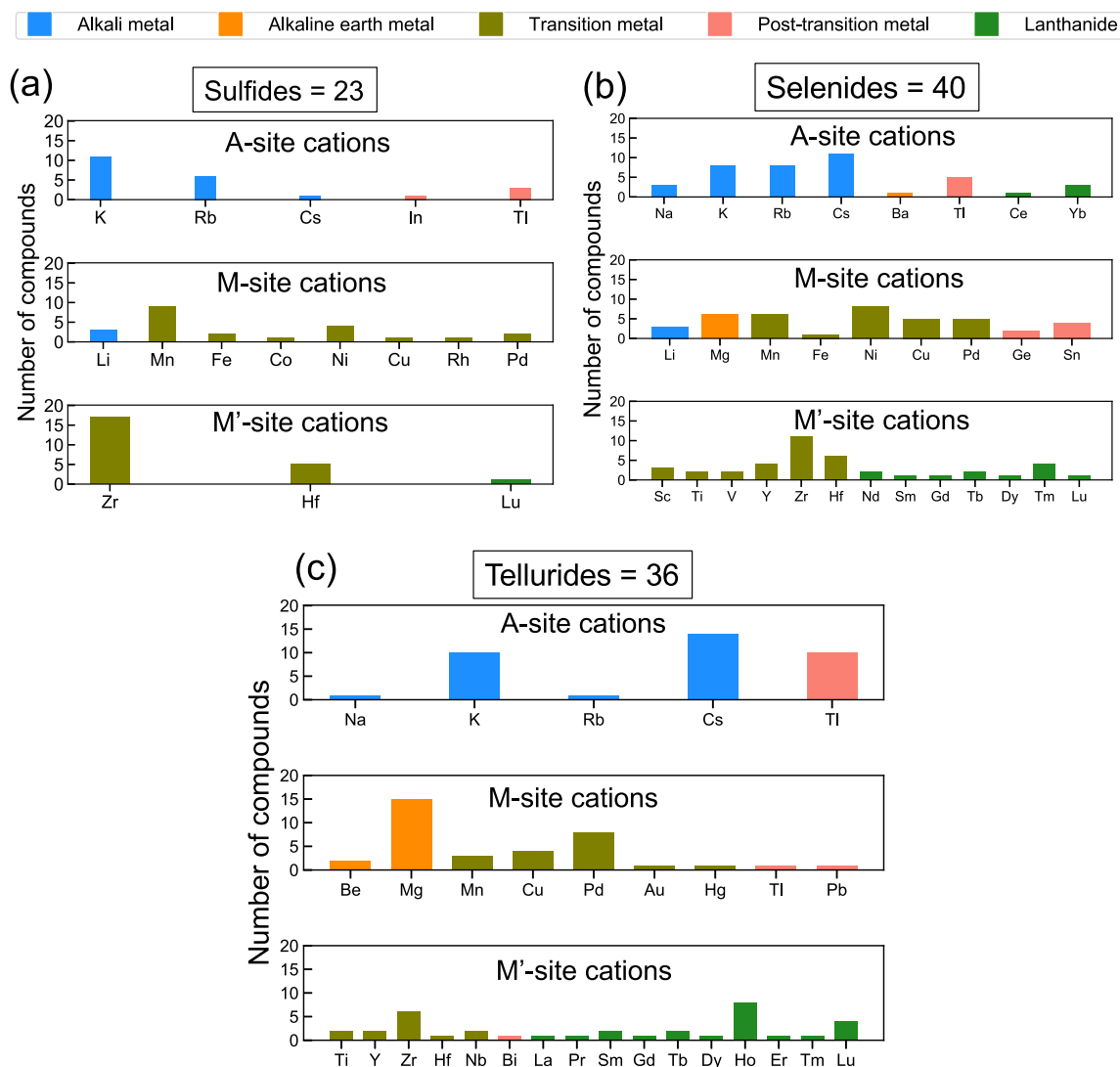


Fig. 4 Elemental distributions of the predicted stable compounds. The cations occupying the A-, M-, and M'-sites in the predicted stable quaternary chalcogenides are shown as bar charts. The height of each bar represents the number of stable compounds that contain the element. There are a total number of 99 predicted stable compounds that consist of **a** 23 sulfides, **b** 40 selenides, and **c** 36 tellurides.

0.17 Wm⁻¹K⁻¹) value of κ_l at 300 K. To understand the origin of ultralow κ_l in this family of materials and to unravel the structure–property relationship, we picked one compound KLiZrSe₃ to investigate its harmonic and anharmonic lattice dynamical properties in detail. In addition to thermodynamic and lattice dynamic stabilities, we checked that KLiZrSe₃ is also thermally stable at 300 K using ab initio molecular dynamics simulation (see Supplementary Note 1 and Supplementary Fig. 4).

We start the analysis of KLiZrSe₃ by examining its phonon dispersion and density of states that are shown up to 225 cm⁻¹ here. For a full phonon dispersion, see Supplementary Fig. 3. We see that the phonon dispersion (Fig. 6a) exhibits (a) very soft (<25 cm⁻¹) acoustic phonon branches along Γ -Y and Γ -Z directions, (b) several low-energy optical phonon modes near 35 cm⁻¹, and (c) a strong hybridization between the phonon branches up to 225 cm⁻¹ (Fig. 6b). To understand the mode-wise contribution to κ_l , we plot the cumulative values of κ_l^{\parallel} , κ_l^{\perp} , and their first-order derivatives (i.e., $\kappa_l^{\parallel\prime}$ and $\kappa_l^{\perp\prime}$) as a function of the phonon frequency in KLiZrSe₃. Figure 6c shows that κ_l^{\parallel} varies up to 45 cm⁻¹ and then plateaus above that frequency, indicating that only the acoustic and low-energy optical phonons up to a frequency of 45 cm⁻¹ mainly contribute to it. On the other hand,

the variation of κ_l^{\perp} occurs up to 135 cm⁻¹ before saturating to a nearly constant value. Hence, the high-energy optical phonons also contribute to κ_l^{\perp} . This anisotropy between κ_l^{\parallel} and κ_l^{\perp} originates from the disparate strength of interlayer and intralayer interactions in the layered crystal structure of KLiZrSe₃, the former being much weaker than the latter. Figure 6d shows small group velocities (<5 km/s) of the phonon modes. Due to their linear dispersion, acoustic phonon branches exhibit the largest group velocity close to 5 km/s, which decreases as the phonon frequency increases. The calculated elastic moduli of KLiZrSe₃ are very low (bulk modulus: 28 GPa, shear modulus: 20 GPa) that give rise to an average sound velocity of 2.48 km/s, which is lower than the average speeds of sound (3.199–4.307 km/s) of the ternary oxides in the Ln₃NbO₇ (Ln = Dy, Er, Y, and Yb)⁵¹ family that also possesses very low κ_l (1.0–1.4 Wm⁻¹K⁻¹ at T = 300 K).

Next, we calculate the mode Gruneisen parameters ($\gamma_{qv} = -\frac{d\ln\omega_{qv}}{dV}$) of the phonon modes in KLiZrSe₃, where ω_{qv} is the frequency of the phonon mode v at the q-point and V is the volume of the unit cell. γ_{qv} 's directly measure the anharmonicity of the phonon modes that play a crucial role in inducing low κ_l in crystalline solids⁵². The calculated γ_{qv} 's of KLiZrSe₃ are very large, with the values reaching as high as 150 for the soft acoustic phonon modes (Fig. 6e). The optical

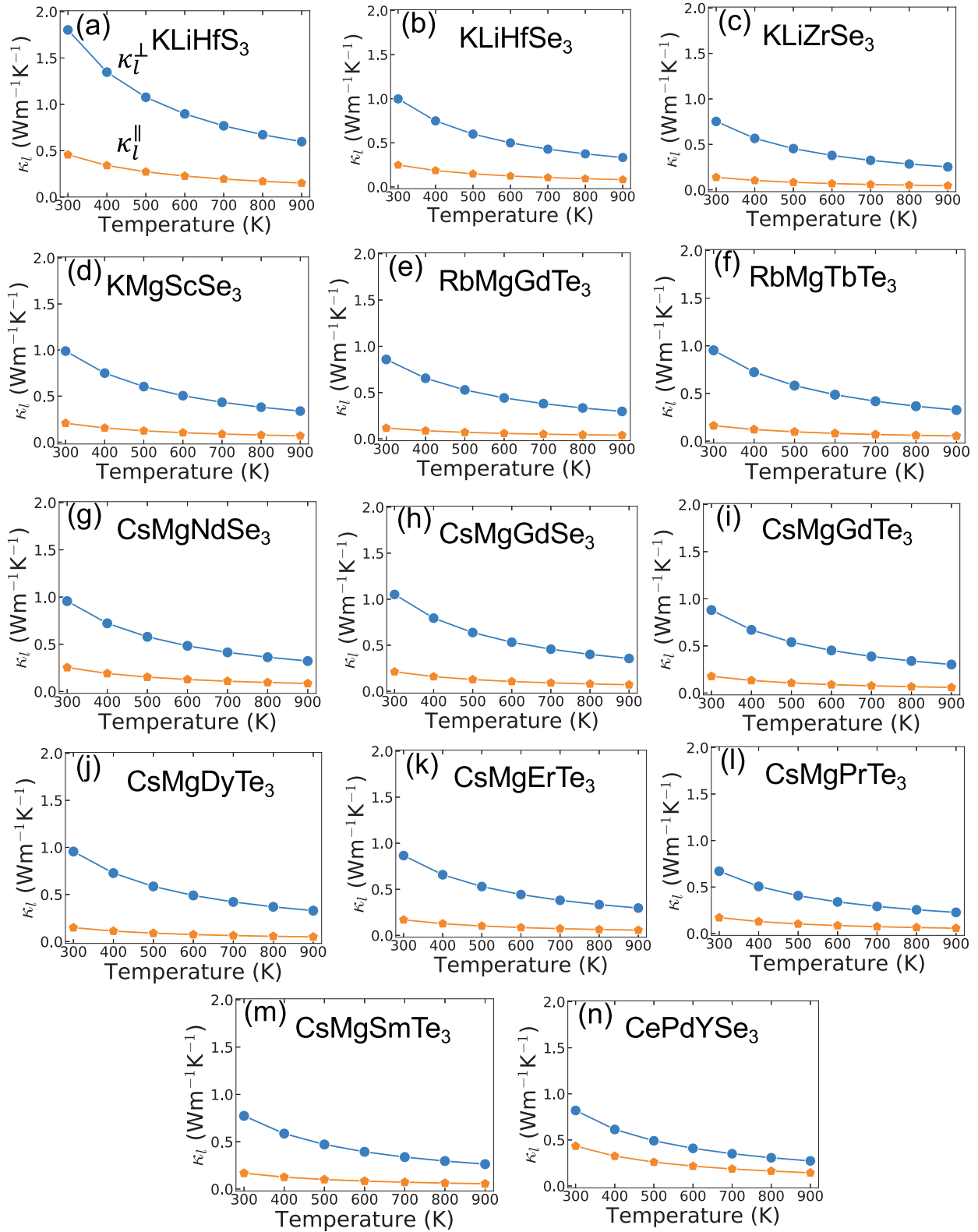


Fig. 5 Thermal-transport properties of the predicted stable compounds. Calculated temperature-dependent lattice thermal conductivity (κ_l) of the 14 compounds that are selected randomly from the predicted stable and semiconducting quaternary chalcogenides—**a** KLiHfS₃, **b** KLiHfSe₃, **c** KLiZrSe₃, **d** KMgScSe₃, **e** RbMgGdTe₃, **f** RbMgTbTe₃, **g** CsMgNdSe₃, **h** CsMgGdSe₃, **i** CsMgGdTe₃, **j** CsMgDyTe₃, **k** CsMgErTe₃, **l** CsMgPrTe₃, **m** CsMgSmTe₃, **n** CePdYSe₃. κ_l^{\parallel} (orange pentagons) and κ_l^{\perp} (blue circles) indicate the components of κ_l parallel and perpendicular to the stacking direction of the layers in the crystal structure of these compounds, respectively.

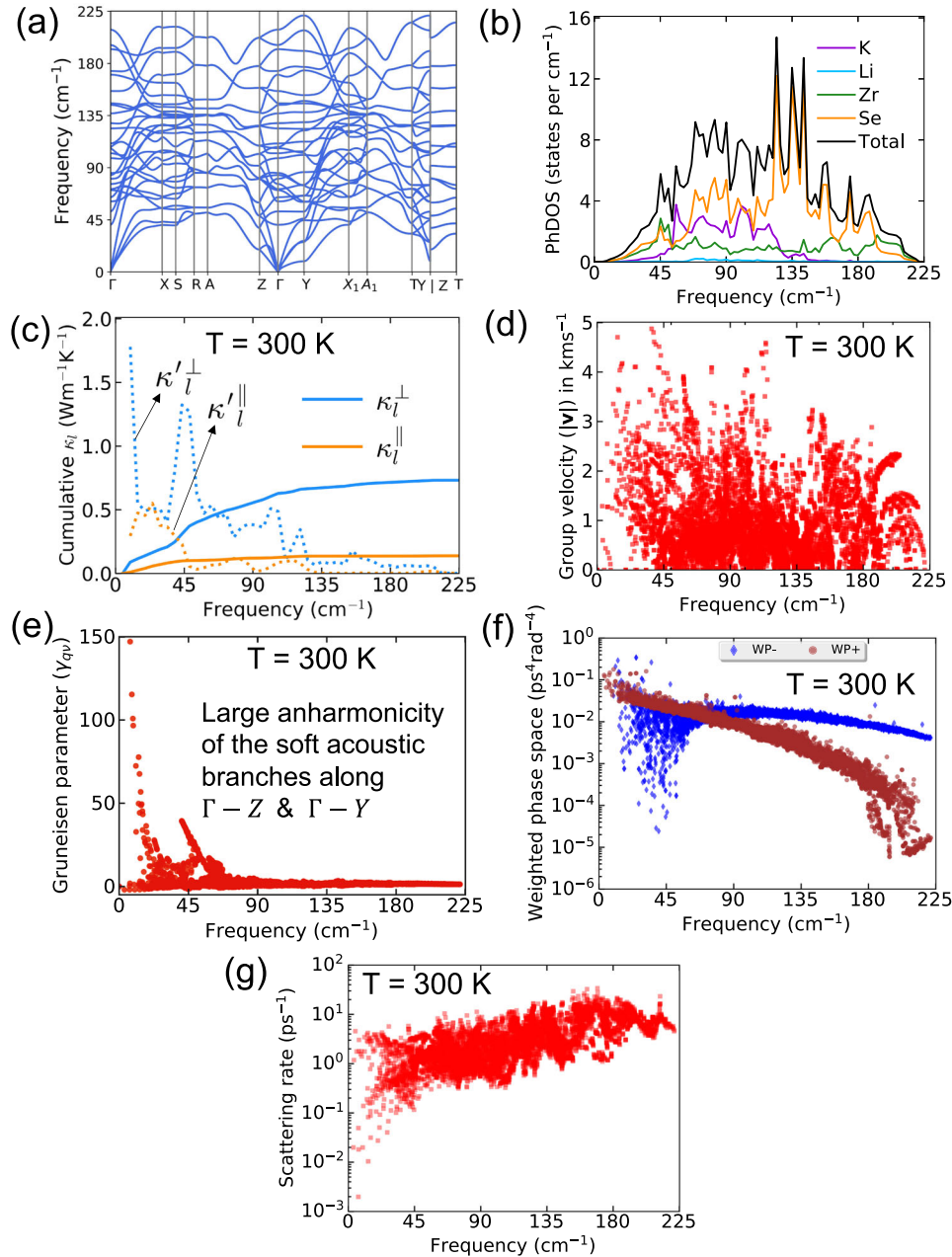


Fig. 6 Harmonic and anharmonic lattice dynamics properties of KLiZrSe₃. **a** Harmonic phonon dispersion and **(b)** density of states of KLiZrSe₃ shown up to 225 cm⁻¹. **c** Cumulative lattice thermal-conductivity plots κ_l^+ and κ_l^- (values are on the y axis) and their first-order derivatives ($\kappa_l^{\prime+}$ and $\kappa_l^{\prime-}$, in arbitrary units) with respect to the phonon frequency, which are obtained from the anharmonic lattice-dynamics calculations. **d** Group velocities (v) of the phonon modes, **(e)** mode Gruneisen parameters (γ_{qv} 's), **(f)** weighted phase (WP) space of the three-phonon-scattering events, where WP+ and WP- indicate the absorption and emission processes, respectively, and **(g)** three-phonon-scattering rates of the phonon frequencies (up to 225 cm⁻¹) obtained using the third-order IFCs.

phonon frequencies (up to 80 cm⁻¹) also exhibit very large γ_{qv} 's ($\gg 1$). As phonon-scattering rate is proportional to γ_{qv}^2 , those low-energy phonons exhibit large scattering rates up to 10 ps⁻¹ (Fig. 6g), which is comparable to that of Sn₂As₂Se₅⁵³, a material that is predicted to have ultralow κ_l (0.37 Wm⁻¹K⁻¹ at T = 300 K). Due to such high values of γ_{qv} the scattering phase space of KLiZrSe₃ becomes very large, leading to enhanced phonon-scattering events, and hence an ultralow value of κ_l in KLiZrSe₃ and this family of compounds in general. We note that κ_l has been calculated here using only the three-phonon-scattering rates. Inclusion of additional scatterings due to higher-order phonon interactions⁵⁴ or grain boundaries⁵⁵ may further decrease the calculated κ_l .

Figure 6a also exhibits a nearly dispersionless optical phonon branch near 48 cm⁻¹ along the X-S-R-A-Z direction, which is reminiscent of rattling vibrations that also help in reducing the phonon lifetimes in this compound. Due to the presence of strong coupling between the acoustic and the low-energy optical phonon modes, the phonon-scattering phase space becomes very large, indicating an enhanced number of scattering processes that are available to those phonon modes. For example, the weighted phase (WP) space (Fig. 6f) for the three-phonon-scattering processes (absorption and emission) becomes larger than 0.1 ps⁴/rad⁴ for low-energy phonons and remains high up to 48 cm⁻¹. Thus, the WP space for these phonons becomes even higher than the filled skutterudite

$\text{YbFe}_4\text{Sb}_{12}$ ⁵⁶, an ultralow- κ_i ($1.18 \text{ W m}^{-1} \text{ K}^{-1}$ at $T = 300 \text{ K}$) material for which the weighted phase space is limited below $0.01 \text{ ps}^4/\text{rad}^4$. It is worth noting that in $\text{YbFe}_4\text{Sb}_{12}$, Yb acts as a rattler atom. Due to the enhanced scattering phase space of the phonon modes up to 225 cm^{-1} , the scattering rates (Fig. 6g) for those phonons also become very high ($>10 \text{ ps}^{-1}$), giving rise to ultralow κ_i in this compound. We provide the mode Gruneisen parameters, group velocities, scattering phase space, and three-phonon-scattering rates for the phonon modes of all 14 compounds in Supplementary Fig. 5–Supplementary Fig. 18. It is interesting to note that the electronic structures (Supplementary Fig. 2) of these compounds exhibit flat-and-dispersive bands as well as multiple-band extrema near the valence- and conduction-band edges, making them attractive for thermoelectric studies.

DISCUSSION

We construct an advanced ML model based on the recently developed iCGCNN model to search for novel compounds by exploring the vast composition space engulfed by a class of known quaternary chalcogenides $\text{AMM}'\text{Q}_3$. The model is designed to be scale-invariant to the input crystal structures, allowing the model to predict the properties of hypothetical compounds more accurately without knowing their DFT-relaxed volumes. Using DFT as a validation tool, we discover a large number of 99 thermodynamically stable and 362 low-energy metastable compounds that are amenable to experimental synthesis and characterization in the laboratory. The overall success rate ($\sim 11\%$) of materials discovery is quite high in our work since we discovered a total number of 461 potentially synthesizable novel quaternary chalcogenides performing DFT calculations for 4199 unique $\text{AMM}'\text{Q}_3$ compositions. To investigate the thermal-transport properties, we randomly select 14 DFT-stable semiconducting and nonmagnetic compounds to calculate their κ_i using the PBTE, including the three-phonon-scattering rates. Our calculations reveal that all of these compounds exhibit ultralow κ_i . By analyzing the harmonic (e.g., phonon dispersion and density of states) and anharmonic (e.g., mode Gruneisen parameters, phonon-scattering phase space) lattice dynamical properties of one of the compounds KLiZrSe_3 , we found that the ultralow κ_i in this family of compounds arises from (a) soft acoustic phonon branches that give rise to low sound velocities, (b) the strong hybridization between the phonon branches appearing at low frequency, and (c) large phonon anharmonicity as evident in the very high values of the mode Gruneisen parameters. The two latter factors help in increasing the phonon-scattering phase space as well as the phonon-scattering rates in this compound. Furthermore, the presence of low-energy nearly dispersionless optical phonon branches, which are reminiscent of rattling phonon branches, also play an important role in giving rise to the small lifetime of the heat-carrying phonons, leading to a very low κ_i . We hope that our work would encourage the application and development of ML models based on graph neural network for the efficient discovery of novel materials. While our model bypasses the need to utilize the DFT-relaxed volume information of the input crystal structures, additional work must be done to design an ML model that can account for the changes that occur in crystal structures during relaxation in terms of the stress and the ionic positions. Last but not least, our results present opportunities in further experimental and theoretical investigations of these newly discovered $\text{AMM}'\text{Q}_3$ materials having innate ultralow κ_i for various thermal-energy management applications.

METHODS

ML-code implementation

The ML-code was implemented based on the existing iCGCNN framework⁴⁶. PyTorch⁵⁷ was used to implement the neural-network components of our model, while Pymatgen⁵⁸ was used for performing the Voronoi tessellations of the crystal structures⁴⁹ before constructing the crystal graphs.

ML training data

Our ML model was trained on DFT-calculated thermodynamic data taken from the OQMD^{14,17} and a previous constrained HT-DFT search of $\text{AMM}'\text{Q}_3$ -type compounds conducted by Pal et al.⁴⁵. Approximately 430,000 unique ordered inorganic compounds with formation energies less than 5 eV/atom were taken from the OQMD. These include experimentally known compounds from the inorganic crystal-structure database (ICSD)⁵⁹ and hypothetical compounds with commonly occurring structures. The HT-DFT study by Pal et al.⁴⁵ was performed for 4659 compounds in various $\text{AMM}'\text{Q}_3$ structure types. All 4659 compounds were included in the ML training data. The crystal graphs of all compounds in the training data were generated from their relaxed crystal structures. For all ML training in this study, 20% of the training data were randomly chosen and reserved for validation.

We note that although there were only 4659 DFT-calculated $\text{AMM}'\text{Q}_3$ compounds and their formation energies in the training data, the search space (i.e., test set) that was explored in this work is much larger (823,680 compounds). However, this lack of data on the $\text{AMM}'\text{Q}_3$ compounds is well supplemented by another $\sim 425,000$ unique entries from the OQMD, which covers a wide range of compositions and crystal structures. While the compounds from the OQMD do not explicitly have the same structures as the $\text{AMM}'\text{Q}_3$ compounds, including these entries helps graph neural-network-based models, such as CGCNN, to learn how attributes of different compositional and structural combinations of the element types correlate with the material property of interest, which in our study is the formation energy. Thus, even though the previously calculated 4659 $\text{AMM}'\text{Q}_3$ compounds do not cover all the different combinations of elements that occur in our targeted search space of 823,680 compounds, the CGCNN model is capable of extrapolating the formation energy of the compounds in our search space by projecting the knowledge that it had learned from entries in the OQMD to the $\text{AMM}'\text{Q}_3$ structures.

DFT calculations

All DFT calculations were performed using the Vienna Ab-initio Simulation Package (VASP)⁶⁰ employing the projector-augmented wave (PAW)^{61,62} potentials. The Perdew–Burke–Ernzerhof (PBE)⁶³ generalized-gradient approximation (GGA) was used to treat the exchange and correlation energies of the electrons. All relaxation and static calculations of the compounds for phase-stability analysis were performed in accordance with the DFT settings as laid out in our high-throughput framework available with the OQMD through the `qmpy` suite of codes^{14,17}.

Stability analysis

We determined the thermodynamic phase stability of the compounds by utilizing the DFT-calculated total energy ($T = 0 \text{ K}$). It has been shown that 0 K thermodynamic phase stability data can often serve as an excellent metric of the synthesizability of a compound^{12,13,17,30,64–68}. To assess the stability of a new quaternary composition we constructed its convex hull by considering all its competing phases in that phase space. From this, we define the stability of a compound by its hull distance (E_{hd}). For a stable compound, by definition, $E_{\text{hd}} = 0$. On the other hand, a compound is considered to be metastable when its E_{hd} lies within 50 meV/atom above the hull in keeping with the heuristic conventions used in literature^{64,69,70}. Compounds that have E_{hd} larger than 50 meV/atom above the hull are considered to be unstable. For a detailed discussion on the convex-hull construction and hull distance, we refer to Refs. 14–17,45,71. It is worth mentioning that many known compounds in the ICSD are metastable with varying positive hull distances^{65,72}.

Calculation of lattice thermal conductivity

We calculated the phonon dispersions of these compounds using $2 \times 2 \times 1$ supercells within the finite-displacement method as implemented in Phonopy⁷³. The high-symmetry paths in the Brillouin zones are adopted following the conventions used by Setyawan et al.⁷⁴ while plotting the phonon dispersions as well the electronic structures. We calculated the lattice thermal conductivity (κ_i) utilizing the phonon life times obtained from the third order interatomic force constants (IFCs)^{75–77}, which was shown to reproduce κ_i within 5% of the experimentally measured κ_i in this $\text{AMM}'\text{Q}_3$ family of compounds^{40,41}. We constructed the third-order IFCs using the compressive sensing lattice dynamics (CSLD) method^{77,78} that utilizes the displacement–force data generated from supercell configurations. In this study, we used $2 \times 2 \times 1$ supercells with the cutoff radius (r_c) for the third-order IFCs taken to be the sixth nearest-neighbor distance within each crystal structure.

Using the second- and third-order IFCs in the ShengBTE code⁷⁹, we calculated the temperature-dependent κ_l utilizing an iterative solution to the Peierls-Boltzmann transport equation (PBTE) for phonons using a $12 \times 12 \times 12$ q-point mesh. It is known that the calculated κ_l depends on r_c , which specifies the maximum range of interaction in the third-order IFCs⁸⁰ as well as on the q-point grid. In our earlier work⁴⁰, we showed that good convergence of κ_l was obtained by limiting r_c even to the third nearest neighbor and with the above mesh of q-points in this family of compounds. Due to the layered crystal structure of the AMM'Q₃ compounds, we present the in-plane (κ_l^+ , which is the directional average of the κ_l components along the two in-plane directions) and the cross-plane (κ_l^{\perp} , which is along the stacking direction of the crystal) components of the calculated κ_l tensor in the "Results" section.

Average speed of sound

To obtain the average speed of sound, we first calculated the bulk (B) and shear (G) moduli of the 14 compounds for which we calculated κ_l (Fig. 5) utilizing the elastic tensor calculated in VASP. Utilizing B and G , we calculated the longitudinal (v_L) and transverse (v_T) speed of sounds

$$\begin{aligned} v_L &= \sqrt{(B + \frac{4}{3}G)/\rho} \\ v_T &= \sqrt{G/\rho}, \end{aligned} \quad (5)$$

where ρ is the density of a compound. Next, we calculate the average speed of sound (v_{av}) using the formula⁸¹

$$3v_{av}^{-3} = v_L^{-3} + 2v_T^{-3}. \quad (6)$$

DATA AVAILABILITY

The data that support the findings of the work are in the paper and Supplementary Information. The structures and energetics of the predicted compounds would be made available through the Open Quantum Materials database (OQMD) in a future release. Additional data will be available upon reasonable request.

CODE AVAILABILITY

The custom codes used in this work are available under reasonable request.

Received: 13 September 2021; Accepted: 17 February 2022;

Published online: 24 March 2022

REFERENCES

- Wu, J. et al. Low-thermal-conductivity rare-earth zirconates for potential thermal-barrier-coating applications. *J. Am. Ceram. Soc.* **85**, 3031–3035 (2002).
- Bell, L. E. Cooling, heating, generating power, and recovering waste heat with thermoelectric systems. *Science* **321**, 1457–1461 (2008).
- Li, S. et al. High thermal conductivity in cubic boron arsenide crystals. *Science* **361**, 579–581 (2018).
- Lindsay, L., Brodido, D. & Reinecke, T. First-principles determination of ultrahigh thermal conductivity of boron arsenide: a competitor for diamond? *Phys. Rev. Lett.* **111**, 025901 (2013).
- Tian, F. et al. Unusual high thermal conductivity in boron arsenide bulk crystals. *Science* **361**, 582–585 (2018).
- Samanta, M., Pal, K., Waghmare, U. V. & Biswas, K. Intrinsically low thermal conductivity and high carrier mobility in dual topological quantum material, n-type bite. *Angew. Chem.* **132**, 4852–4859 (2020).
- Mukhopadhyay, S. et al. Two-channel model for ultralow thermal conductivity of crystalline tl3vse4. *Science* **360**, 1455–1458 (2018).
- Xia, Y., Pal, K., He, J., Ozoliņš, V. & Wolverton, C. Particlelike phonon propagation dominates ultralow lattice thermal conductivity in crystalline tl3vse4. *Phys. Rev. Lett.* **124**, 065901 (2020).
- Biswas, K. et al. High-performance bulk thermoelectrics with all-scale hierarchical architectures. *Nature* **489**, 414 (2012).
- Zhao, L.-D. et al. Ultralow thermal conductivity and high thermoelectric figure of merit in snse crystals. *Nature* **508**, 373 (2014).
- Slade, T. J. et al. Contrasting snse-nasbte2 and snse-nabite2 thermoelectric alloys: High performance facilitated by increased cation vacancies and lattice softening. *J. Am. Chem. Soc.* **142**, 12524–12535 (2020).
- Curtarolo, S. et al. The high-throughput highway to computational materials design. *Nat. Mater.* **12**, 191–201 (2013).

- Jain, A., Shin, Y. & Persson, K. A. Computational predictions of energy materials using density functional theory. *Nat. Rev. Mater.* **1**, 1–13 (2016).
- Saal, J. E., Kirklin, S., Aykol, M., Meredig, B. & Wolverton, C. Materials design and discovery with high-throughput density functional theory: the open quantum materials database (OQMD). *JOM* **65**, 1501–1509 (2013).
- Jain, A. et al. Commentary: the materials genome approach to accelerating materials innovation. *APL Mater.* **1**, 011002 (2013).
- Curtarolo, S. et al. Aflowlib.org: A distributed materials properties repository from high-throughput ab initio calculations. *Comput. Mater. Sci.* **58**, 227–235 (2012).
- Kirklin, S. et al. The open quantum materials database (OQMD): assessing the accuracy of DFT formation energies. *npj Comput. Mater.* **1**, 1–15 (2015).
- Rupp, M. Machine learning for quantum mechanics in a nutshell. *Int. J. Quantum Chem.* **115**, 1058–1073 (2015).
- Ward, L., Agrawal, A., Choudhary, A. & Wolverton, C. A general-purpose machine learning framework for predicting properties of inorganic materials. *npj Comput. Mater.* **2**, 16028 (2016).
- Faber, F. A., Lindmaa, A., Von Lilienfeld, O. A. & Armiento, R. Machine learning energies of 2 million elpasolite (A B C 2 D 6) crystals. *Phys. Rev. Lett.* **117**, 135502 (2016).
- Faber, F., Lindmaa, A., von Lilienfeld, O. A. & Armiento, R. Crystal structure representations for machine learning models of formation energies. *Int. J. Quantum Chem.* **115**, 1094–1101 (2015).
- Hautier, G., Fischer, C. C., Jain, A., Mueller, T. & Ceder, G. Finding nature's missing ternary oxide compounds using machine learning and density functional theory. *Chem. Mater.* **22**, 3762–3767 (2010).
- Tabor, D. P. et al. Accelerating the discovery of materials for clean energy in the era of smart automation. *Nat. Rev. Mater.* **3**, 5–20 (2018).
- Meredig, B. et al. Combinatorial screening for new materials in unconstrained composition space with machine learning. *Phys. Rev. B* **89**, 094104 (2014).
- Balachandran, P. V. et al. Predictions of new ab o 3 perovskite compounds by combining machine learning and density functional theory. *Phys. Rev. Mater.* **2**, 043802 (2018).
- Ramprasad, R., Batra, R., Pilania, G., Mannodi-Kanakkithodi, A. & Kim, C. Machine learning in materials informatics: recent applications and prospects. *npj Comput. Mater.* **3**, 1–13 (2017).
- Ward, L. & Wolverton, C. Atomistic calculations and materials informatics: a review. *Curr. Opin. Solid State Mater. Sci.* **21**, 167–176 (2017).
- Ren, F. et al. Accelerated discovery of metallic glasses through iteration of machine learning and high-throughput experiments. *Sci. Adv.* **4**, eaaq1566 (2018).
- Kim, K. et al. Machine-learning-accelerated high-throughput materials screening: discovery of novel quaternary heusler compounds. *Phys. Rev. Mater.* **2**, 123801 (2018).
- Gautier, R. et al. Prediction and accelerated laboratory discovery of previously unknown 18-electron abx compounds. *Nat. Chem.* **7**, 308 (2015).
- He, J., Naghavi, S. S., Hegde, V. I., Amsler, M. & Wolverton, C. Designing and discovering a new family of semiconducting quaternary heusler compounds based on the 18-electron rule. *Chem. Mater.* **30**, 4978–4985 (2018).
- Koscielski, L. A. & Ibers, J. A. The structural chemistry of quaternary chalcogenides of the type AMM'Q₃. *Z. Anorg. Allg. Chem.* **638**, 2585–2593 (2012).
- Strobel, S. & Schleid, T. Three structure types for strontium copper (i) lanthanide (iii) selenides SrCuMSe₃ (M= La, Gd, Lu). *J. Alloys Compd.* **418**, 80–85 (2006).
- Ruseikina, A. V. et al. Synthesis, structure, and properties of EuErCu₃. *J. Alloys Compd.* **805**, 779–788 (2019).
- Maier, S. et al. Crystal structures of the four new quaternary copper (i)-selenides A_{0.5}CuZrSe₃ and ACuYSe₃ (A= Sr, Ba). *J. Solid State Chem.* **242**, 14–20 (2016).
- Ruseikina, A. V., Andreev, O. V., Galenko, E. O. & Koltsov, S. I. Trends in thermodynamic parameters of phase transitions of lanthanide sulfides SrLnCu₃ (Ln=La–Lu). *J. Therm. Anal. Calorim.* **128**, 993–999 (2017).
- Ruseikina, A., Solov'ev, L., Galenko, E. & Grigor'ev, M. Refined crystal structures of SrLnCu₃ (Ln=Er, Yb). *Russ. J. Inorg. Chem.* **63**, 1225–1231 (2018).
- Sikerina, N. & Andreev, O. Crystal structures of SrLnCu₃ (Ln=Gd, Lu). *Russ. J. Inorg. Chem.* **52**, 581–584 (2007).
- Prakash, J., Mesbah, A., Beard, J. C. & Ibers, J. A. Syntheses and crystal structures of BaAgTb₃, BaCuGdTe₃, BaCuTbTe₃, BaAgTbTe₃, and CsAgUTe₃. *Z. Anorg. Allg. Chem.* **641**, 1253–1257 (2015).
- Pal, K., Xia, Y., He, J. & Wolverton, C. Intrinsically low lattice thermal conductivity derived from rattler cations in an AMM'Q₃ family of chalcogenides. *Chem. Mater.* **31**, 8734–8741 (2019).
- Hao, S. et al. Design strategy for high-performance thermoelectric materials: The prediction of electron-doped KZrCuSe₃. *Chem. Mater.* **31**, 3018–3024 (2019).
- Pal, K., Xia, Y., He, J. & Wolverton, C. High thermoelectric performance in baagyte 3 via low lattice thermal conductivity induced by bonding heterogeneity. *Phys. Rev. Mater.* **3**, 085402 (2019).
- Pal, K., Hua, X., Xia, Y. & Wolverton, C. Unraveling the structure-valence-property relationships in AMM'Q₃ chalcogenides with promising thermoelectric performance. *ACS Appl. Energy Mater.* **3**, 2110–2119 (2019).

44. Fabini, D. H., Koerner, M. & Seshadri, R. Candidate inorganic photovoltaic materials from electronic structure-based optical absorption and charge transport proxies. *Chem. Mater.* **31**, 1561–1574 (2019).
45. Pal, K. et al. Accelerated discovery of a large family of quaternary chalcogenides with very low lattice thermal conductivity. *npj Comput. Mater.* **7**, 1–13 (2021).
46. Park, C. W. & Wolverton, C. Developing an improved crystal graph convolutional neural network framework for accelerated materials discovery. *Phys. Rev. Mater.* **4**, 063801 (2020).
47. Xie, T. & Grossman, J. C. Crystal graph convolutional neural networks for an accurate and interpretable prediction of material properties. *Phys. Rev. Lett.* **120**, 145301 (2018).
48. Bartel, C. J. et al. A critical examination of compound stability predictions from machine-learned formation energies. *npj Comput. Mater.* **6**, 1–11 (2020).
49. Ward, L. et al. Including crystal structure attributes in machine learning models of formation energies via voronoi tessellations. *Phys. Rev. B* **96**, 024104 (2017).
50. Wu, D. et al. Direct observation of vast off-stoichiometric defects in single crystalline sncse. *Nano Energy* **35**, 321–330 (2017).
51. Yang, J. et al. Diffused lattice vibration and ultralow thermal conductivity in the binary Ln–Nb–O oxide system. *Adv. Mater.* **31**, 1808222 (2019).
52. Morelli, D., Jovovic, V. & Heremans, J. Intrinsically minimal thermal conductivity in cubic I–V–VI₂ semiconductors. *Phys. Rev. Lett.* **101**, 035901 (2008).
53. Gan, Y., Huang, Y., Miao, N., Zhou, J. & Sun, Z. Novel IV–V–VI semiconductors with ultralow lattice thermal conductivity. *J. Mater. Chem. C* **9**, 4189–4199 (2021).
54. Xia, Y. et al. High-throughput study of lattice thermal conductivity in binary rocksalt and zinc blende compounds including higher-order anharmonicity. *Phys. Rev. X* **10**, 041029 (2020).
55. Pal, K., Xia, Y. & Wolverton, C. Microscopic mechanism of unusual lattice thermal transport in tin telluride. *npj Comput. Mater.* **7**, 1–8 (2021).
56. Li, W. & Mingo, N. Ultralow lattice thermal conductivity of the fully filled skutterudite YbFe₄Sb₁₂ due to the flat avoided-crossing filler modes. *Phys. Rev. B* **91**, 144304 (2015).
57. Paszke, A. et al. Pytorch: an imperative style, high-performance deep learning library. *Adv. Neural Inf. Process. Syst.* **32**, 8024–8035 (2019).
58. Ong, S. P. et al. Python materials genomics (pymatgen): a robust, open-source python library for materials analysis. *Comput. Mater. Sci.* **68**, 314–319 (2013).
59. Belsky, A., Hellenbrandt, M., Karen, V. L. & Luksch, P. New developments in the inorganic crystal structure database (ICSD): accessibility in support of materials research and design. *Acta Crystallogr., Sect. B: Struct. Sci.* **58**, 364–369 (2002).
60. Kresse, G. & Furthmüller, J. Efficiency of ab-initio total energy calculations for metals and semiconductors using a plane-wave basis set. *Comp. Mater. Sci.* **6**, 15–50 (1996).
61. Blöchl, P. E. Projector augmented-wave method. *Phys. Rev. B* **50**, 17953 (1994).
62. Kresse, G. & Joubert, D. From ultrasoft pseudopotentials to the projector augmented-wave method. *Phys. Rev. B* **59**, 1758 (1999).
63. Perdew, J. P., Burke, K. & Ernzerhof, M. Generalized gradient approximation made simple. *Phys. Rev. Lett.* **77**, 3865 (1996).
64. Zakutayev, A. et al. Theoretical prediction and experimental realization of new stable inorganic materials using the inverse design approach. *J. Am. Chem. Soc.* **135**, 10048–10054 (2013).
65. Aykol, M., Dwaraknath, S. S., Sun, W. & Persson, K. A. Thermodynamic limit for synthesis of metastable inorganic materials. *Sci. Adv.* **4**, eaaq0148 (2018).
66. Anand, S., Wood, M., Xia, Y., Wolverton, C. & Snyder, G. J. Double half-Heuslers. *Joule* **3**, 1226–1238 (2019).
67. Hautier, G., Jain, A. & Ong, S. P. From the computer to the laboratory: materials discovery and design using first-principles calculations. *J. Mater. Sci.* **47**, 7317–7340 (2012).
68. Sun, W. et al. Thermodynamic routes to novel metastable nitrogen-rich nitrides. *Chem. Mater.* **29**, 6936–6946 (2017).
69. Cerqueira, T. F. et al. Identification of novel Cu, Ag, and Au ternary oxides from global structural prediction. *Chem. Mater.* **27**, 4562–4573 (2015).
70. Wu, Y., Lazić, P., Hautier, G., Persson, K. & Ceder, G. First principles high throughput screening of oxynitrides for water-splitting photocatalysts. *Energy Environ. Sci.* **6**, 157–168 (2013).
71. Emery, A. A., Saal, J. E., Kirklın, S., Hegde, V. I. & Wolverton, C. High-throughput computational screening of perovskites for thermochemical water splitting applications. *Chem. Mater.* **28**, 5621–5634 (2016).
72. Sun, W. et al. The thermodynamic scale of inorganic crystalline metastability. *Sci. Adv.* **2**, e1600225 (2016).
73. Togo, A. & Tanaka, I. First principles phonon calculations in materials science. *Scr. Mater.* **108**, 1–5 (2015).
74. Setyawan, W. & Curtarolo, S. High-throughput electronic band structure calculations: Challenges and tools. *Comp. Mater. Sci.* **49**, 299–312 (2010).
75. Chaput, L., Togo, A., Tanaka, I. & Hug, G. Phonon-phonon interactions in transition metals. *Phys. Rev. B* **84**, 094302 (2011).
76. Togo, A., Chaput, L. & Tanaka, I. Distributions of phonon lifetimes in Brillouin zones. *Phys. Rev. B* **91**, 094306 (2015).
77. Zhou, F., Nielson, W., Xia, Y. & Ozoliņš, V. Lattice anharmonicity and thermal conductivity from compressive sensing of first-principles calculations. *Phys. Rev. Lett.* **113**, 185501 (2014).
78. Zhou, F., Nielson, W., Xia, Y. & Ozoliņš, V. Compressive sensing lattice dynamics. I. general formalism. *Phys. Rev. B* **100**, 184308 (2019).
79. Li, W., Carrete, J., Katcho, N. A. & Mingo, N. ShengBTE: a solver of the Boltzmann transport equation for phonons. *Comp. Phys. Comm.* **185**, 1747–1758 (2014).
80. Li, C. W. et al. Orbital driven giant phonon anharmonicity in SnSe. *Nat. Phys.* **11**, 1063 (2015).
81. Christensen, M. et al. Avoided crossing of rattler modes in thermoelectric materials. *Nat. Mater.* **7**, 811 (2008).

ACKNOWLEDGEMENTS

The authors acknowledge support from the U.S. Department of Energy under Contract No. DE-SC0014520 (thermal-conductivity calculations), National Institute of Standards and Technology as part of the Center for Hierarchical Materials Design (CHiMaD) under the Award 70NANB19H005 by U.S. Department of Commerce (HT-DFT calculations), the Toyota Research Institute through the Accelerated Materials Design and Discovery program (machine learning and lattice dynamics), and the National Science Foundation through the MRSEC program (NSF-DMR 1720139) at the Materials Research Center (phase stability). We acknowledge the computing resources provided by (a) the National Energy Research Scientific Computing Center (NERSC), a U.S. Department of Energy Office of Science User Facility operated under Contract No. DE-AC02-05CH11231, (b) Quest High-Performance Computing Facility at Northwestern University, which is jointly supported by the Office of the Provost, the Office for Research, and Northwestern University Information Technology, and (c) the Extreme Science and Engineering Discovery Environment (National Science Foundation Contract ACI-1548562).

AUTHOR CONTRIBUTIONS

K.P. conceived and designed the project. K.P. performed HT-DFT calculations and analysis with suggestions from Y.X., J.S., and C.W. C.W.P. designed and trained the ML model, and performed ML predictions with suggestions from C.W. C.W. supervised the whole project. All authors discussed the results, provided comments, and contributed to writing the paper. K.P. and C.W.P. contributed equally to this work.

COMPETING INTERESTS

The authors declare no competing interests.

ADDITIONAL INFORMATION

Supplementary information The online version contains supplementary material available at <https://doi.org/10.1038/s41524-022-00732-8>.

Correspondence and requests for materials should be addressed to Koushik Pal, Cheol Woo Park or Chris Wolverton.

Reprints and permission information is available at <http://www.nature.com/reprints>

Publisher's note Springer Nature remains neutral with regard to jurisdictional claims in published maps and institutional affiliations.



Open Access This article is licensed under a Creative Commons

Attribution 4.0 International License, which permits use, sharing, adaptation, distribution and reproduction in any medium or format, as long as you give appropriate credit to the original author(s) and the source, provide a link to the Creative Commons license, and indicate if changes were made. The images or other third party material in this article are included in the article's Creative Commons license, unless indicated otherwise in a credit line to the material. If material is not included in the article's Creative Commons license and your intended use is not permitted by statutory regulation or exceeds the permitted use, you will need to obtain permission directly from the copyright holder. To view a copy of this license, visit <http://creativecommons.org/licenses/by/4.0/>.

© The Author(s) 2022